

Article

A Hierarchical Classification Framework of Satellite Multispectral/Hyperspectral Images for Mapping Coastal Wetlands

Leilei Jiao ¹, Weiwei Sun ^{1,*}, Gang Yang ^{1,2}, Guangbo Ren ³ and Yinnian Liu ⁴

¹ Department of Geography and Spatial Information Techniques, Ningbo University, Ningbo 315211, China; 1711073007@nbu.edu.cn (L.J.); yanggang@nbu.edu.cn (G.Y.)

² State Key Laboratory of Remote Sensing Science, Institute of Remote Sensing and Digital Earth, Chinese Academy of Sciences, Beijing 100101, China

³ First Institute of Oceanography, Ministry of Natural Resources of China, Qingdao 266061, China; renguangbo@fio.org.cn

⁴ Key Laboratory of Infrared System Detection and Imaging Technologies, Shanghai Institute of Technical Physics, Chinese Academy of Sciences, Shanghai 200083, China; ynliu@mail.sitp.ac.cn

* Correspondence: sunweiwei@nbu.edu.cn; Tel.: +86-182-5879-6120

Received: 17 August 2019; Accepted: 23 September 2019; Published: 26 September 2019



Abstract: Mapping different land cover types with satellite remote sensing data is significant for restoring and protecting natural resources and ecological services in coastal wetlands. In this paper, we propose a hierarchical classification framework (HCF) that implements two levels of classification scheme to identify different land cover types of coastal wetlands. The first level utilizes the designed decision tree to roughly group land covers into four rough classes and the second level combines multiple features (i.e., spectral feature, texture feature and geometric feature) of each class to distinguish different subtypes of land covers in each rough class. Two groups of classification experiments on Landsat and Sentinel multispectral data and China Gaofen (GF)-5 hyperspectral data are carried out in order to testify the classification behaviors of two famous coastal wetlands of China, that is, Yellow River Estuary and Yancheng coastal wetland. Experimental results on Landsat data show that the proposed HCF performs better than support vector machine and random forest in classifying land covers of coastal wetlands. Moreover, HCF is suitable for both multispectral data and hyperspectral data and the GF-5 data is superior to Landsat-8 and Sentinel-2 multispectral data in obtaining fine classification results of coastal wetlands.

Keywords: hierarchical classification framework; coastal wetlands; Landsat images; hyperspectral imagery; Sentinel-2; GF-5

1. Introduction

Coastal wetlands are characterized as remarkable and crucial systems located in the transition zone between terrestrial land and ocean [1,2]. They perform a wide range of ecological functions including reducing coastal erosion, preserving environment health, removing nutrient and suspended solid, adjusting local climate, providing habitats and refuges for fish and wildlife [3–5]. Unfortunately, dramatic degradation in the area of coverage, ecological value and biodiversity has occurred in the worldwide coastal wetlands over the past decades, which severely increases the vulnerability of coastal wetlands [6,7]. The main reasons come from global sea-level rise [8,9] and inappropriate anthropogenic activities [10]. Therefore, it is an urgent work to map spatial distribution and dynamic changes of land covers in coastal wetlands, in order to restore and protect natural resources and ecological services in coastal environments.

The complicated and vulnerable ecosystems of coastal wetlands make the traditional manual investigation could not work in realistic applications, because many coastal wetlands are inaccessible for humans and field measurements are difficult and time consuming [11,12]. Satellite remote sensing techniques provide an important and effective data source for mapping and monitoring coastal wetlands, because of its unique characteristics in an easy data acquisition, spatially continuous coverage and short revisiting periods [4,13,14]. During the last several decades, the fast development of satellite remote sensing sensors has greatly enhanced our capability to map coastal wetlands, that is, panchromatic sensors [13,15], Synthetic Aperture Radar (SAR) [16], multispectral sensors [17,18] and even hyperspectral imagers [19,20]. Conventional panchromatic sensors could not discriminate different species in coastal wetlands (e.g., vegetation) because of their single limited band information [21]. SAR has strong penetration but its data processing work is complicated and its inversion of biomass is more limited than optical remote sensing [5]. Satellite multispectral images like Landsat TM/ETM+, Gaofen-1 WVF, Sentinel-2A and advanced spaceborne Thermal Emission and Reflection Radiometer (ASTER), have more advantages in monitoring coastal wetland habitats, because of their moderate spatial resolution, wide spatial coverage and multiple optical bands [22,23]. They could identify main types of land covers, that is, water, farmland and woodland but could not distinguish vegetation communities, for example, different subtypes of swamps. Accordingly, it is a big challenge to achieve a fine classification map of coastal wetlands. Combing multispectral sensors with other sensors like SAR and Lidar might integrate respective advantages of these sensors and it has shown some promising results in mapping coastal wetlands [24–26]. On the other hand, the imaging spectrometer could provide numerous narrow spectral bands at each pixel [27]. The high spectral resolution (<10 nm) of hyperspectral images renders that it owns greater potentials in identifying different ground objects of coastal wetlands with subtle spectral divergence [28,29]. Some hyperspectral sensors have been utilized in mapping coastal wetlands, for example, Earth Observing-1 (EO-1) Hyperion [20], Hyperspectral InfraRed Image (HypIRI) [19], Compact High Resolution Imaging Spectrometer (CHRIS) [30] and Hyperspectral Imager for the Coastal Ocean (HICO) [31].

The divergences in spectral characteristics within multispectral and hyperspectral images could reflect different ground objects [32]. Accordingly, researchers tried to utilize the spectral information to identify different land covers of coastal wetlands. For example, the work of spectral analysis on five wetland classes by Meisam Amani show that Near-Infrared (NIR), Red Edge (RE) and red bands are top three most useful bands for separating different wetland classes, whereas Shortwave Infrared (SWIR) and green bands have poorer separability [33]. Elhadi Adam analyzed the ASD field spectrometer data and found that there are statistically significant differences in spectral reflectance between papyrus and its co-existing species on 412 wavelengths located in different portions of the electromagnetic spectrum [34]. René R. Colditz explored 14 spectral indices and their appropriate thresholds for water mapping in coastal wetlands and told us that MODIS green (band 4) and short wave infrared (band 6) “MNDWI6” perform the best of all [35]. Moreover, supervised classifiers are usually employed to make the pixel-based classification on spectral signatures, for example, Statistical classifiers like maximum likelihood classifier (MLC) [13] and machine learning like support vector machine (SVM) [36] and random forest (RF) [37]. Reschke combined multi-temporal Landsat imagery with high resolution satellite data and adopted the RF algorithm to extract subpixel information of coastal wetland classes [38]. Petropoulos proposed a semi-automatic classification based on SVM to classify different spectral responses of Landsat TM images and quantify the deposition and erosion in two Mediterranean wetland deltas [39]. Pierre Dubeau investigated the potential of optical remote sensing images for mapping the primary vegetation groups in the Dabus Wetlands using the non-parametric RF classifier [40]. However, the pixel-based classification result is always limited by the complicated landscape with diverse land-cover types and their small patch sizes [41]. Moreover, spectral variations in spatial locations make that different species in coastal wetlands might have similar spectral signatures [27]. The single source of spectral information accordingly could not distinguish

mixed species composition of wetlands and often leads to comparatively low mapping accuracies and class confusions of specific classes, for example, paddy and swamp, croplands and shrublands.

The idea of object-based image analysis was then introduced into classifying remote sensing images of coastal wetlands [42]. It considers the spatial location and context of homogeneous pixels and integrates multiple spatial features to promote the classification accuracy. The object-based classifier groups objects that have similar spatial features, for example, a similar pixel shape, color or texture and classify them based on the object features. Berberoglu extracted the vegetation information using Grey Level Co-occurrence Matrix (GLCM) and explored the land cover change dynamics of a Mediterranean coastal wetland [43]. Jia adopted an object-oriented classification method on Landsat data to map the spatial distribution of mangrove areas in coastal wetlands of China and obtained accurate results [44]. Wang explored the potentials of completed local binary patterns (CLBP) in extracting texture feature and applied it to classify vegetation in Yancheng coastal wetlands of China [45]. Unfortunately, determining proper spatial-object features is time consuming and the performance of object-based classifier might diverge greatly across different features selected.

Furthermore, it will be natural to wonder whether one can combine spectral information with spatial-object information to upgrade the classification result, because they are complementary to each other. The idea of spatial-spectral based classification has been investigated in remote sensing image processing, where spatial features are extracted from the original images and stacked with spectral signatures to carry out classification. Many popular algorithms can be used to extract spatial features, for example, extended morphological profiles (EMP) [46], attribute profiles (AP) [47] and Markov random fields (MRF) [48]. However, the above schemes treated remote sensing data as a regular image and the good performance highly relies on the complicated parameter tuning work of spatial operators. Moreover, they did not involve the essential expert rules extracted from spectral variables of specific land cover types. For example, the brightness index (BI) from Tasseled Cap transformation can be well distinguish built-up areas from non-built up areas.

Inspired from the decision tree, the purpose of our study is to present a simple and effective framework for mapping coastal wetlands from multispectral and hyperspectral images. The decision tree does not require assumptions concerning the frequency distribution of spectral data in each land cover type [49]. We then would like to involve the information of expert rules of spectral variables and spatial-object information into the framework and promote the classification of mapping coastal wetlands. We implement multispectral data from Landsat TM/ETM+/OLI sensors because of their typical features of free to access, long archived history and widely used status [50]. On 9 May 2018, China successfully launched the Gaofen-5 (GF-5) satellite, which takes an advanced hyperspectral sensor. The GF-5 advanced hyperspectral imaged (AHSI) has 330 spectral bands ranging from 400 to 2500 nm and is designed to provide users hyperspectral data with higher spectral resolution and larger swath width. Unfortunately, mapping capacity of GF-5 hyperspectral data has not been investigated in classifying coastal wetlands. Therefore, our study focuses on the following two key objectives: (1) to develop a hierarchical classification framework (HCF) for mapping coastal wetlands from satellite multispectral and hyperspectral images; and (2) to investigate the mapping capabilities of Landsat and GF-5 remote sensing data in classifying different land covers of coastal wetlands.

Compared to previous work, our paper favors three scientific contributions. First, the idea of two-level HCF is different and advantageous to current methods. In the first level, the implemented expert rules of spectral indices for 4 rough classes and the structure of decision tree are specifically designed and different from current methods. In the second level, the spectral, geometric and texture features are carefully chosen for coastal wetland mapping. Second, our proposed HCF is easy to implement and flexible in mapping different land covers in coastal wetlands, which works well on either multispectral or hyperspectral images. Third, we are the first to demonstrate that the GF-5 hyperspectral data have clear advantages in coastal mapping than multispectral images like Landsat and Sentinel data.

2. Materials and Methods

2.1. Study Area

Two study areas of coastal wetlands in Figure 1 were selected in our study because of their abundant land cover types of coastal wetlands, that is, the Yellow River estuary and the Yancheng coastal wetland in China.

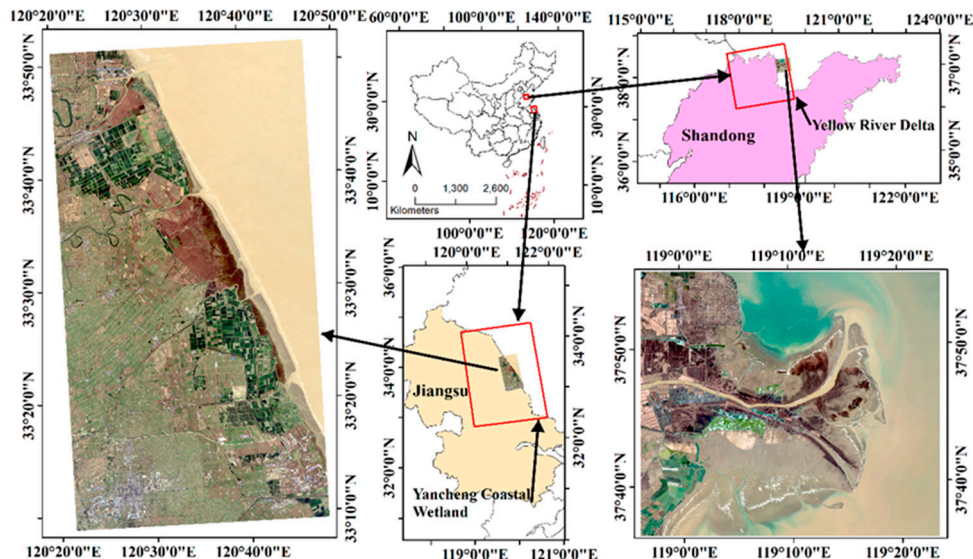


Figure 1. Location of our study areas.

The Yellow River Delta is the fastest growing delta in the world [51], which is located in the northeast of Shandong Province, China ($36^{\circ}55'$ – $38^{\circ}16'$ N, $117^{\circ}31'$ – $119^{\circ}18'$ E). Its northern and eastern regions are adjacent to the Bohai Bay and the Laizhou Bay [52]. It has a temperate monsoon climate, the annual mean temperature is 11.9°C and the average precipitation and pan evaporation are about 640 mm and 1500 mm with 196 frostless days, respectively [53]. It has abundant coastal wetland resources and has been named as one of the most beautiful six wetlands in China [54]. The Yellow River Estuary, located in the east of the Yellow River Delta, was selected as our study area, with the total area $2.424 \times 103 \text{ km}^2$. The land covers of this study area is strongly influenced by salinization processes and the vegetation mainly composes of halophytic plant communities dominated by grass and shrub species. The richness of land cover types makes it an ideal test sites for mapping coastal wetlands.

Yancheng coastal wetland is located in east of Jiangsu Province, China ($32^{\circ}34'$ – $34^{\circ}28'$ N, $119^{\circ}27'$ – $121^{\circ}16'$ E), having jurisdiction over Xiangshui, Binhai, Sheyang, Dafeng and Dongtai five cities, with the coastline length 582 km and an area of $4.553 \times 103 \text{ km}^2$ [55]. It has a monsoon climate, receiving rich rainfall and solar radiation energy. The annual average temperature is between 13.7°C and 14.8°C , the annual precipitation is 900–1100 mm and the elevation is between 0 and 4 m, with an average slope of less than 5 degrees [56]. Various ecological types exist in the tidal flat wetlands, which mainly compose of clay and silt fine particulate matter, due to the suitable hydrological and climatic conditions. This area is rich in natural wetland resources, with a large area of radiating sandbars, coastal forest farms and grasslands and a wide coastal beach is the habitat of a variety of state-level key protected animals and plants. Yancheng wetland reserve was certified as a national nature reserve (Yancheng National Nature Reserve, YNNR) in 1992, joined the international biosphere reserve under UNESCO's Man and the Biosphere Programme (MAB) in 1993 and was designated as Ramsar Convention List of Wetlands of International Importance in 2002 [57]. In this paper, the YNNR and its expanded area are selected as another study area.

2.2. Datasets

In this study, we implement satellite remote sensing images from Landsat-5 Thematic mapper (TM), Landsat-7 Enhanced Thematic Mapper (ETM+) and Landsat-8 Operational Land Imager (OLI) from the period of 2001–2015 and GF-5 AHSI of 2018 to carry out classification experiments in two study areas of coastal wetlands. The Landsat images were archived on the Earth Resources Observation and Science (EROS) Center (<http://glovis.usgs.gov/>). The Sentinel images were acquired free from the Copernicus Open Access Hub (<https://scihub.copernicus.eu/>). The GF-5 AHSI image was provided by the Shanghai institute of physics and technology, Chinese academy of sciences.

Landsat TM data have 7 spectral bands, with a spatial resolution of 30 m for bands 1–5 and 7; TM band 6 (thermal infrared) is acquired at 120 m spatial resolution. The Landsat ETM+ data consist of 6 spectral bands with a spatial resolution of 30 m for bands 1–5 and 7; ETM+ band 6 (thermal infrared) is acquired at 60 m resolution and band 8 (panchromatic band) has a resolution of 15 m. The Landsat OLI data have 8 spectral bands with a spatial resolution of 30 m for bands 1–7 and 9, 1 panchromatic band with spatial resolution of 15 m for band 8 and 2 thermal infrared bands with a spatial resolution of 100 m for bands 10 and 11 [58].

The Sentinel MSI data have 13 spectral bands, with a spatial resolution of 10 m for bands 2–4 and 8, band 5–7 (RE band) and band 11–12 (SWIR) has a resolution of 20 m and band 1(coastal aerosol), band 9 (Water vapor) and band 10 (Cirrus) with a spatial resolution of 60 m [59].

The AHSI is the main payload of the GF-5 satellite and is developed by Shanghai Institute of Technical Physics, Chinese Academy of Science. AHSI is designed to be capable of resolving 330 spectral bands from 400 to 2500 nm with 30 m spatial resolution and 60 km swath width. The spectral resolution is about 5 nm for VNIR (400–1000 nm) and 10 nm for SWIR (1000–2500 nm). AHSI is China's first spaceborne hyperspectral imager with a convex grating spectrum. Compared to the instruments on board like Hyperion, AHSI has a much higher signal-to-noise ratio (about 3–4 times), a much wider swath width (about 8 times) and much more spectral bands (more than 100).

The acquisition time of GF-5 hyperspectral data is November, 2018 and it is the first GF-5 imagery on Yellow River Estuary all over the world. We then chose the winter images for all involved datasets and selected the images closest to the collective data of GF-5. The reason for that is to keep the time consistency and reduce the negative effects from the changing land cover types in classification results of different images. Table 1 list the information of satellite remote sensing data. We select Landsat TM (2010), Landsat ETM+ (2005) and Landsat OLI (2015) for the two areas. Moreover, we select Landsat multispectral data (2018), Sentinel-2 multispectral data (2018) and GF-5 hyperspectral data (2018) of the Yellow River Estuary area to investigate their difference in the classification performance.

Table 1. List of satellite images used in this study.

Study Areas	Satellite Data	Sensors	Track Number	Time	Spatial Resolutions
Yellow River Estuary	Landsat-5	TM	121/034	2010/12/16	30 m
	Landsat-7	ETM+	121/034	2005/12/26	30 m
	Landsat-8	OLI	121/034	2015/01/12	30 m
	Landsat-8	OLI	121/034	2018/11/20	30 m
	Sentinel-2	MSI	206/132	2018/10/24	10/20 m
	GF-5	AHSI	002/571	2018/11/01	30 m
Yancheng coastal wetland	Landsat-5	TM	119/037	2010/12/18	30 m
	Landsat-7	ETM+	119/037	2001/02/16	30 m
	Landsat-8	OLI	119/037	2015/12/16	30 m

3. Methodology

Figure 2 shows the flowchart of our HCF method for mapping land covers of coastal wetlands. After data processing, the HCF implements two levels of the classification scheme to identify different subtypes of land covers. The first level adopts the expert rules of spectral variables into the decision

tree and groups different land covers into 4 main classes, built-up, cropland, wetlands and vegetation. The second level utilizes the SVM classifier on each rough class and combines spectral features, texture features and geometric features to obtain subtypes of land covers for all four main classes. The classification map of coastal wetlands is finally obtained by combining the classification result of each subtype.

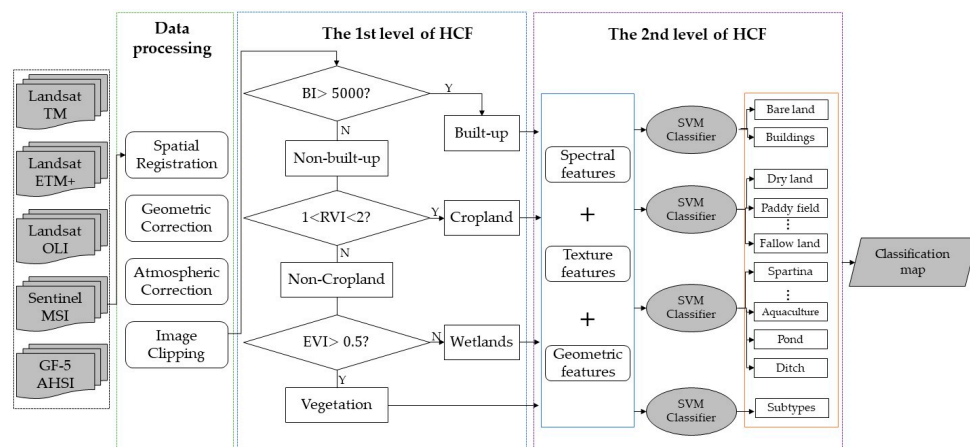


Figure 2. The flowchart of our hierarchical classification framework (HCF).

3.1. Data Preprocessing

Some data processing work is essential before carrying out our HCF method in remote sensing images, including spatial registration, geometric correction, atmospheric correction and image clipping. All the three datasets are transformed into the WGS 84 geographic coordinate system. Landsat data is used as the reference image for spatially registering GF-5 AHSI images and Sentinel-2 data. The controlling points are evenly collected across the image scene to guarantee the spatial error less than one pixel. GF-5 hyperspectral imagery is geometrically corrected using the 30 m global DEM data (<https://asterweb.jpl.nasa.gov/gdem.asp>) and the Rational Polynomial Coefficient files and the bilinear interpolation method is then employed to resample the image data. The Sentinel-2 was also resampled to 30 m by using the nearest neighbor sampling to match the spatial resolutions of Landsat-8 and GF-5 AHSI data. All the raw images with digital numbers were calibrated to surface reflectance. Bad and noisy bands in GF-5 AHSI data are removed, that is [1,2,193–204,246–265,269–271,323–330] and the left 285 bands were used in our experiments. Atmospheric correction of all datasets was made by using the Fast Line-of-Sight Atmospheric Analysis of Spectral Hypercubes (FLAASH) module of ENVI software. The self-adaptive local regression model was implemented to repair the scan line errors of Landsat ETM+ images. Radiometric calibration on GF-5 hyperspectral data is carried out by using the gain and offset coefficients. The satellite data on both study areas are clipped from original images by overlying vector files in the study areas.

3.2. The First Level of HCF

The first level of HCF implements a decision tree to make coarse classification of coastal wetlands. Land covers of coastal wetlands can be roughly grouped into four main classes: built-up, vegetation, cropland and wetlands. Unfortunately, croplands and wetlands might have similar spectral curves and could not be well differentiated from each other, for example, the paddy in croplands and the pond in wetlands. Meanwhile, the croplands have similar spectral responses with vegetation, especially in summer. It will be a challenging work for well recognizing them by implementing the classification scheme on spectral curves. Therefore, we adopt the idea of decision tree to formulate a “from top to down” multistage scheme to successively recognize four main classes. Our designed decision tree makes a binary decision to separate the complicated decision into three simpler decisions and that leads to a better interpretation of identifying different land covers.

The first layer of the decision tree separates built-up area from other three classes. Brightness part of Tasseled Cap transformation has been proven to provide a good measure of building density for built-up areas in the remote sensing images [60]. Therefore, we adopt the Tasseled Cap transformation and implement the BI in Equation (1) to identify built-up areas.

$$\text{BI} = 0.2909 \times \text{B_BLUE} + 0.2493 \times \text{B_GREEN} + 0.4806 \times \text{B_RED} + 0.5568 \times \text{B_NIR} + 0.4438 \times \text{B_SWIR1} + 0.1706 \times \text{B_SWIR2} \quad (1)$$

where B_BLUE, B_GREEN, B_RED, B_NIR, B_SWIR1 and B_SWIR2 are blue, green, red, near-infrared, the first short-wave infrared and the second short-wave infrared bands respectively. They correspond to band 1 (450–520 nm), band 2 (520–600 nm), band 3 (630–690 nm), band 4 (760–900 nm), band 5 (1550–1750 nm) and band 7 (2090–2350 nm) in Landsat TM/ETM+/OLI images. For GF-5 AHSI images, we summarize the bands within all band wavelength intervals of Landsat data and average them to obtain the six combined bands. The average of bands 15–18 (450.23–505.86 nm) represents the combined blue band. The average of bands 34–47 (531.5–587.2 nm) represents the combined green band. The average of bands 60–66 represents the combined red band. The average of bands 109–115 (852.3–877.9 nm) represents the combined near-infrared band. The average of bands 69–77 (1577.6–1645.5 nm) represents the first short-wave infrared bands and the average of bands 133–153 (2116.9–2285.7 nm) represents the second short-wave infrared bands. We then extract the built-up area by segmenting the BI image with a manual threshold and the threshold is set to be 5000 after our trial experiments. If $\text{BI} > 5000$, it will be regarded to be built-up area; otherwise, it belongs to non-built-up.

And then, we implement the second layer of decision tree on the non-built-up area to identify croplands. Previous studies show that the ratio vegetation index (RVI) can well reflect the difference of vegetation coverage and growth status, particularly for vegetation with high coverage and vigorous growth [61]. Therefore, we adopt the RVI to identify croplands from non-built-up area, which is defined as following:

$$\text{RVI} = \text{B_NIR}/\text{B_RED} \quad (2)$$

Our trail experience shows that the RVI of croplands is usually greater than 1 but smaller than 2. Therefore, we manually extract the cropland within the RVI interval and set others in non-built-up area to be non-cropland.

After that, we separate vegetation and wetlands from non-croplands. Enhanced Vegetation Index (EVI) has been proven to be a good measure to extract the vegetation [62]. Our trial experience shows that vegetation has much higher EVI values than wetlands, especially in the coastal area. We accordingly compute EVI and differentiate vegetation from wetlands. The EVI is defined as follows:

$$\text{EVI} = 2.5 \times (\text{B_NIR} - \text{B_RED}) / (\text{B_NIR} + 6 \times \text{B_RED} - 7.5 \times \text{B_BLUE} + 1) \quad (3)$$

Using the binary segmentation scheme, we divide the non-croplands into vegetation and wetlands. The threshold is set to be 0.5 after our numerous trials. If $\text{EVI} > 0.5$, the corresponding pixels are labeled as vegetation; otherwise, they are grouped into wetlands. And the four classes of land covers in coastal wetlands are finally obtained.

3.3. The Second Level of HCF

The second level of HCF is to divide each class into different sub-classes and obtain the fine classification map. According to International Convention on wetlands, the built-up area comprises of bare land and buildings; croplands comprises of dry land, paddy, fallow land and so on; wetlands comprises of spartina, reed, aquaculture, pond, ditch, marsh and so on; and vegetation comprises of several subtypes, for example, *suaeda* and trees [15,63].

The subtypes of each class has similar spectral features and could not be fully identified by their spectrum divergences. The shape and texture features can help to enrich the information for

classifying different subtypes in each class [64]. For example, the high albedo of buildings is close to that of bare land but buildings have different geometric characteristics with the later, such as shape (length-width ratio, compactness, area) and texture [65]. The dry land, fallow land and paddy in croplands have similar shape features but show divergent texture features [66]. The ponds, especially the dry ponds and mudflats have similar spectral responses but they differ in texture and shape features [23]. The marsh and mudflat in wetlands are always mixed with each other. The spectral variability in spatial locations might bring about their spectrum similarity but fortunately, they show clear differences in the texture [67]. The reed, tamarix chinensis and spartina are always mixed together in coastal wetlands. Their spectral curves are similar with each other but have different patterns in shape and texture [68]. The deep sea and shallow sea in wetlands have similar spectral curves and their texture patterns diverge greatly.

Texture features show spatial variations, spatial correlation and arrangement of grayscales in the image and the gray level cooccurrence matrix (GLCM) is usually used to detect the spatial orientation and amplitude variations of texture features. In this paper, we implement four measures of GLCM texture features, including entropy, homogeneity, contrast, dissimilarity and correlation. The homogeneity measures the inner dissimilarity of objects and low dissimilarity brings about high homogeneity. The contrast quantifies the variations of objects and reveals the anomalies. The correlation describes linear relationships of grayscales in the objects. The dissimilarity characterizes the detailed variations of grayscales in the object. Geometric features show the size and shape information of each object. We use six measures of shape features, including area, length-width ratio, length, width, compactness and density. Table 2 lists the equations of all measures for quantifying texture and shape features. We implement object-oriented method to segment remote sensing images at multi-scale, so that homogeneous pixels can be segmented into objects with different sizes. After that, for each class, we stack the spectral curves, texture features and shape features and utilize the support vector machine (SVM) classifier to identify different subtypes [69,70]. We combine the result of each class and achieve the final classification map of coastal wetlands.

Table 2. The utilized measures of texture and geometric features.

Features	Measures	Equations
Texture features	Homogeneity	$f_{Hom} = \sum_{i,j=0}^{N-1} \frac{P_{i,j}}{1+(i-j)^2} \quad (4)$
	Contrast	$f_{Con} = \sum_{i,j=0}^{N-1} P_{i,j}(i-j)^2 \quad (5)$
	Correlation	$f_{Cor} = \frac{\sum_{i,j=0}^{N-1} P_{i,j} \times (i-f_{mean_i}) \times (j-f_{mean_j})}{\sqrt{f_{var_i} \times f_{var_j}}} \quad (6)$
	Dissimilarity	$f_{Dis} = \sum_{i,j=0}^{N-1} P_{i,j} i - j \quad (7)$
Geometric features	Area	$A = N_O \quad (8)$
	Length-width ratio	$\gamma = \frac{L}{W} = \frac{Eig_1(O)}{Eig_2(O)} \quad (9)$
	Width	$W = \sqrt{\frac{A}{\gamma}} \quad (10)$
	Length	$L = \sqrt{A\gamma} \quad (11)$
	Shape Index	$S = \frac{1}{4\sqrt{A}} \quad (12)$
	Density	$d = \frac{\sqrt{N_O}}{1 + \sqrt{Var(X) + Var(Y)}} \quad (13)$

Notes: N is the number of grayscale levels, (P_{ij}) is the entry in GLCM in line i and column j , f_{Hom} is the homogeneity measure, f_{Con} is the contrast measure and f_{Cor} and f_{Dis} are correlation and dissimilarity measures respectively. f_{mean_i} and f_{var_i} are the average and standard variance of grayscales in line i , N_O is the number of pixels in the object O , $Eig_1(O)$ is the eigenvalue of covariance matrix, A is the area measure, γ is the length-width ratio, L is the length measure and W is the width measure. \lceil is the perimeter of object O , S is the shape index measure, X and Y are vectors stacked from image coordinates of boundary pixels, $Var(X)$ is the variance of X and d is the density measure.

4. Experimental Results

We design two groups of experiments on two study areas in order to comprehensively testify the classification performance of proposed HCF. The first group is to verify the classification behaviors of HCF on the multispectral data by comparing it with two-state-of-the art methods SVM and RF. The second group is to investigate the performance difference of HCF in mapping coastal wetlands with different source data, that is, GF-5 hyperspectral, Sentinel-2 and Landsat multispectral data. Classification accuracy is quantified as kappa coefficient (KC), overall accuracy (OA), producer's accuracy (PA) and user's overall (UA).

4.1. Classification Comparison between SVM, RF and HCF on Landsat Data

In this experiment, we use three images (Landsat-5, Landsat-7 and Landsat-8) of both Yellow River Estuary and Yancheng coastal wetland to testify the classification performance of HCF. The classification results of HCF is compared with those of SVM and RF on the two study areas. To make a fair comparison, the training and testing samples of each Landsat data are independently selected.

4.1.1. Yellow River Estuary

The Yellow river estuary comprises of 13 land cover types including sea, river, built-up, dry land, paddy field, ditch, aquaculture, pond, mudflat, marsh, vegetation, bare land and salt marsh. Using the field survey with global positioning system (GPS) and with the help of high spatial resolution images, we obtain the region of interesting (ROI) of ground truth for all land cover types. The training and testing samples are then randomly selected from the ROI and their detailed information is listed in Table 3. To ensure a fair sampling condition, the number of training samples is almost three times that of testing samples.

Table 3. Training and testing samples of each land cover type for Yellow River estuary Landsat data.

Land Cover Types	2005				2010				2015			
	Training		Testing		Training		Testing		Training		Testing	
	Pixel	ROI	Pixel	ROI	Pixel	ROI	Pixel	ROI	Pixel	ROI	Pixel	ROI
sea	2731	70	910	65	5392	77	1797	57	2019	25	673	25
river	293	56	97	40	332	30	110	30	616	24	205	24
buildings	38	22	12	20	78	22	26	20	95	16	31	16
dry land	183	39	61	26	126	24	42	24	103	20	34	20
paddy field	211	52	70	48	201	31	67	31	116	28	38	28
ditch	129	18	43	20	156	35	52	30	105	17	35	18
aquaculture	332	28	110	25	164	15	54	15	167	18	55	17
pond	191	40	63	39	464	21	154	17	548	16	182	16
mudflat	593	44	197	40	1731	29	577	31	1394	29	464	20
marsh	404	55	134	50	69	19	23	17	110	12	36	14
vegetation	1376	52	458	50	662	49	220	13	314	25	104	25
bare land	109	38	36	23	54	31	18	30	40	19	13	8
salt marsh	71	33	23	26	41	21	13	20	390	18	130	18
Total	6661	547	2214	472	9470	404	3153	335	6017	267	2000	249

Table 4 shows the OA and KC of three classification methods on the Yellow River Estuary Landsat data. The SVM on three periods has OA of 88.7%, 84.33% and 81.37% and KC of 0.85, 0.8 and 0.76, respectively. The RF has OA of 90.46%, 88.77% and 94.19% and KC of 0.82, 0.85 and 0.93, respectively. The OAs of HCF in the three periods is 93.63%, 93.01% and 95.97% and the KCs are 0.91, 0.87 and 0.94, respectively. HCF behaves better than SVM and RF, having higher OA and KC in the three periods of Landsat data. Meanwhile, Figure 3 illustrates the UA and PA from each method. More than eight classes of HCF has over 85% PA and UA in Landsat-7 data, the RF has eight classes exceed 85% and the SVM only has six classes with over 85% PA. The HCF, SVM and RF classification maps of landsat-5 have slightly worse UA and PA than those of the Landsat-7 data. Only seven classes of HCF have the

PA and UA over 85% on the Landsat-5 data, RF has six classes with over 85% PA and only four classes (sea, aquaculture, salt marsh) has higher PA and UA in the SVM classification map. The HCF performs best on the Landsat-8 data, regardless of UA or PA and ten classes of HCF has PA over 90%. The next is RF and eight classes have over 85% PA and UA in Landsat-8 classification map, whereas there were only five classes in the SVM classification map. Misclassifications exist mostly in dry land of 2005, the paddy field of 2010 and the ditch of 2015.

Table 4. Classification accuracies from HCF, SVM and RF on the Yellow river estuary Landsat data.

	Landsat-7			Landsat-5			Landsat-8		
	HCF	SVM	RF	HCF	SVM	RF	HCF	SVM	RF
OA (%)	93.62	88.7	90.46	93.01	84.33	88.77	95.97	81.37	94.19
KC	0.91	0.85	0.82	0.87	0.8	0.85	0.94	0.76	0.93

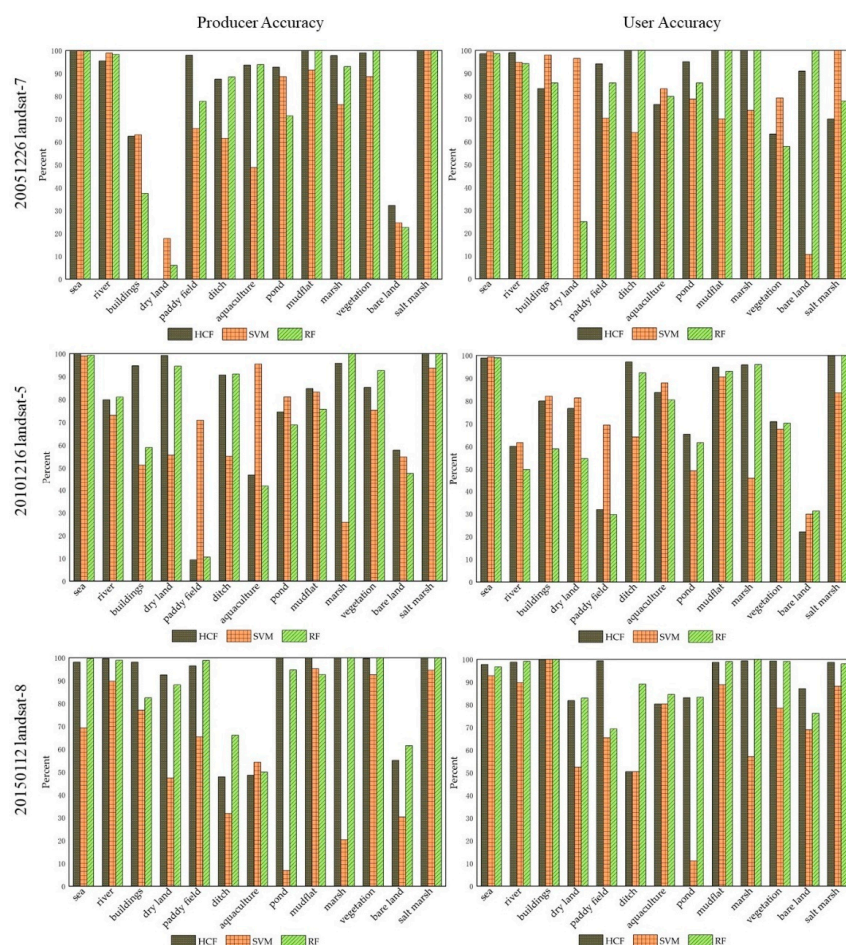


Figure 3. The comparison of producer's accuracy (PA) and user's overall (UA) between HCF, support vector machine (SVM) and random forest (RF) on Yellow River Estuary Landsat data.

Moreover, Figure 4 shows the classification maps of HCF, SVM and RF in the three periods. Land cover types change significantly over time and a lot of land was developed and utilized. The classification results are consistent with the original image. In general, the visual performance of the two methods was roughly the same in each period. A lot of coastal land was developed and utilized from 2005 to 2015. The visual behaviors of classification maps of HCF, SVM and RF are roughly the same in each period. Both methods misclassify salt marshes into marsh on the Landsat-7 data. For the Landsat-5 data, the SVM and RF misclassify salt marsh into river and HCF misclassifies pond into river. Both methods misclassify part of sea into ditch and the SVM brings about a higher misclassification

rate on Landsat-8 data. Overall, the HCF is superior to SVM and RF in classification on the Yellow River Estuary Landsat data. And HCF achieves the best result on the Landsat-8 data, followed by Landsat-7 data.

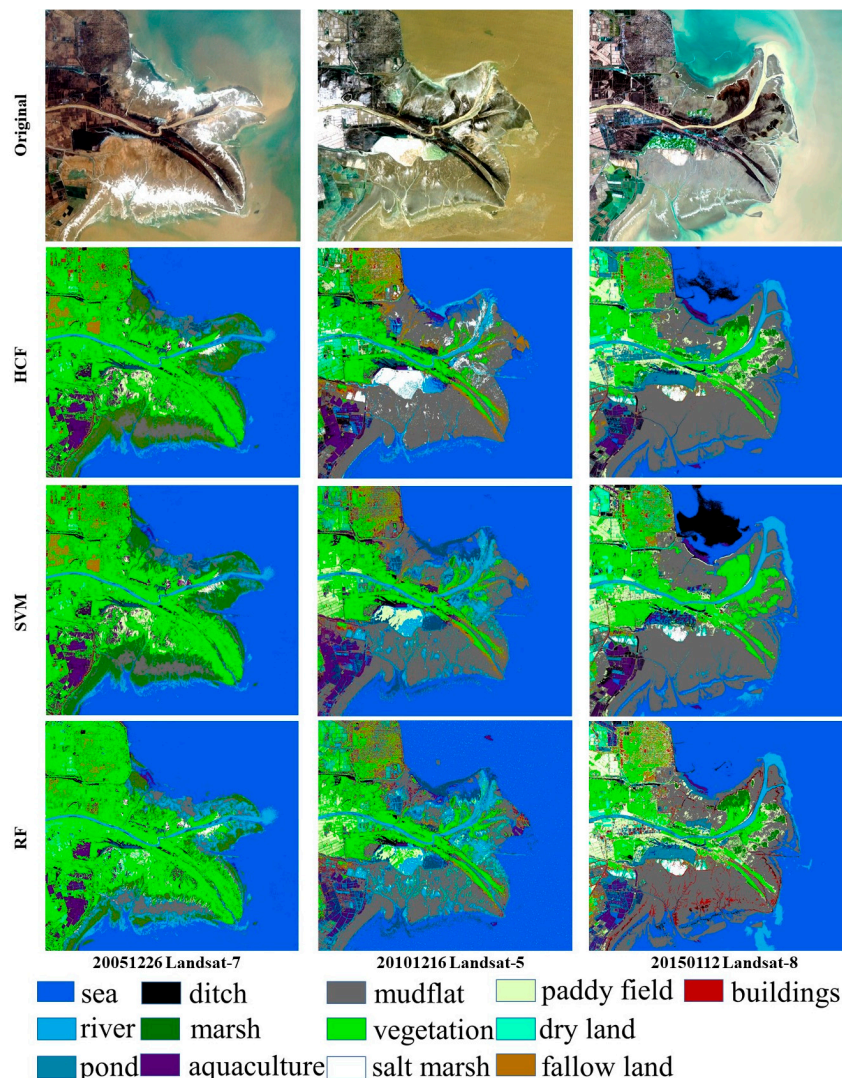


Figure 4. Classification maps of HCF, SVM and RF on the Yellow River Estuary Landsat data.

4.1.2. Yancheng Coastal Wetland

Yancheng coastal wetland consists of 12 land cover types including sea, river, buildings, dry land, ditch, aquaculture, pond, mudflat, marsh, vegetation and fallow land. Table 5 lists the training and testing sample information of Landsat data in the Yancheng coastal wetland. To ensure a fair sampling condition, the number of training samples is almost three times that of testing samples.

Table 6 shows the OA and KC of both methods on the Landsat data of Yancheng coastal wetland. The RF on three periods has OA of 78.76%, 78.39% and 72.41% and KC of 0.75, 0.72 and 0.65, respectively. The SVM has OA of 83.42%, 78.81% and 89.9% and KC of 0.77, 0.73 and 0.86, respectively. The OAs of HCF is 93.46%, 90.1% and 93% and KCs are 0.92, 0.86 and 0.91, respectively. The HCF performs better than SVM and RF on all three Landsat datasets and achieves the best classification accuracy on the Landsat-7 data. The PA and UA of HCF in Figure 5 also supports the above observations. Specifically, HCF has six classes of land covers with over 85% PA and UA in Landsat-7 data, whereas RF and SVM have only four classes. In contrast with Landsat-7 data, all the three methods have slightly worse PA and UA on the Landsat-5 data. The HCF has only four classes with over 85% PA and UA in Landsat-5

data, whereas RF has four classes and SVM has three classes. The HCF classification accuracies on Landsat-8 data perform best of all. It has seven classes with over 90% PA and UA. Moreover, Figure 6 shows the classification maps of HCF, SVM and RF on Yancheng coastal wetland. Land covers changed greatly in the past decade (2001–2015), especially in the first five years. The HCF behaves better than SVM and RF in distinguishing paddy field from dry land and it could identify buildings more accurately, especially on the Landsat-8 data. Therefore, HCF achieves better classification accuracy than SVM and RF in mapping coastal wetlands. HCF achieves the best results on Landsat-8 data, followed by Landsat-7 data, which is consistent with the results in the Yellow River Estuary area.

Table 5. Training and testing samples of 12 land covers for Yancheng coastal wetland.

Land Cover Types	2001				2010				2015			
	Training		Testing		Training		Testing		Training		Testing	
	Pixel	ROI	Pixel	ROI	Pixel	ROI	Pixel	ROI	Pixel	ROI	Pixel	ROI
sea	8216	42	2738	40	3414	49	1138	33	8126	42	2708	45
river	1484	96	494	95	778	69	259	60	1484	96	494	68
buildings	679	60	226	60	656	62	218	62	6185	107	2061	100
dry land	1686	84	562	83	268	61	89	40	1121	66	373	60
paddy field	821	66	273	45	240	73	80	70	727	64	242	50
ditch	243	38	81	38	124	41	41	40	243	38	81	38
aquaculture	245	45	81	45	66	45	22	43	1025	60	341	59
pond	1310	51	436	51	617	20	205	17	767	40	255	35
mudflat	1683	90	561	89	227	40	75	37	1526	34	508	34
marsh	1736	59	578	59	956	32	318	32	1623	37	541	35
vegetation	313	35	104	35	87	29	29	28	468	44	156	44
fallow land	992	70	330	70	190	26	63	19	1078	46	359	40
Total	19408	736	6464	710	7623	547	2537	481	24373	674	8119	608

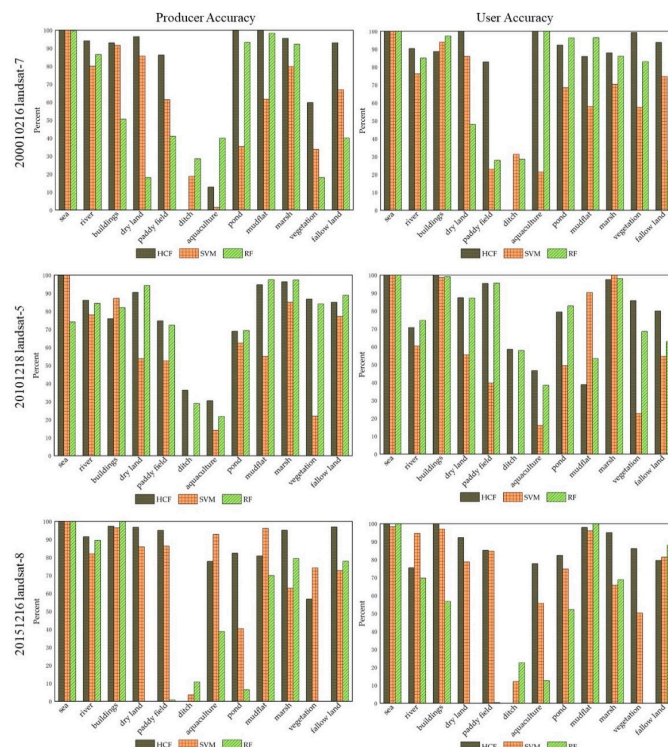
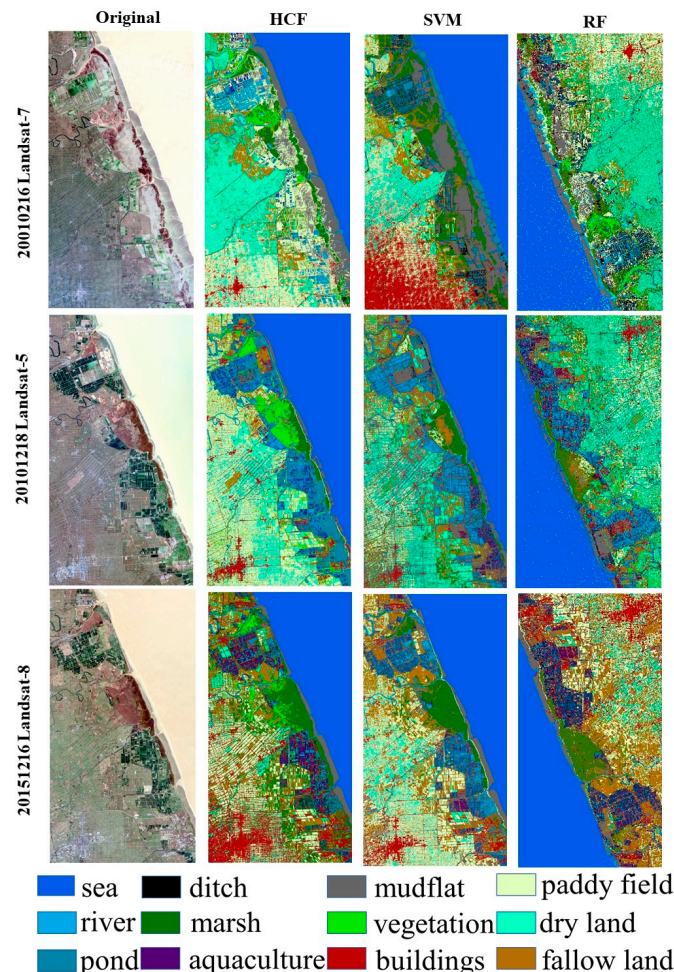


Figure 5. The comparison of PA and UA between HCF, SVM and RF on Yancheng coastal wetland.

Table 6. Classification accuracies of HCF, SVM and RF on Landsat data of Yancheng coastal wetland.

	Landsat-7			Landsat-5			Landsat-8		
	HCF	SVM	RF	HCF	SVM	RF	HCF	SVM	RF
OA (%)	93.46	83.42	78.76	90.1	78.81	78.39	93	89.9	72.41
KC	0.92	0.77	0.75	0.86	0.73	0.72	0.91	0.86	0.65

**Figure 6.** Classification Maps of HCF, SVM and RF on Yancheng coastal wetland Landsat data.

4.2. Classification Comparison between GF-5, Landsat-8 and Sentinel-2 Data

This experiment investigates the difference in classification performance of HCF on GF-5 AHSI, Landsat-8 and Sentinel-2 data. To better demonstrate the capability of different data, we carry out two classification experiments on the Yellow River Estuary and identify 13 coarse classes and 21 fine classes of land covers respectively.

Table 7 shows the OA and KC of 13 land cover types, which include marsh, paddy, dry land, bare land, aquaculture, river, ditch, sea, vegetation, pond, building, mudflat and salt marsh. The OA and KC of the GF-5 AHSI data are 94.98% and 0.93, the Sentinel-2 data are 93.4% and 0.92 and Landsat-8 data are 92.34% and 0.90. GF-5 AHSI data have higher OA and KC than Sentinel-2 and Landsat-8 and Landsat-8 is the worst of three datasets. Figure 7 plots the PA and UA of HCF on GF-5 hyperspectral data, Landsat-8 and Sentinel-2 multispectral data. The Landsat-8 and Sentinel-2 have more than eight classes with over 75% UA, whereas GF-5 has more than ten classes. Figure 8 shows classification map of HCF on the three datasets. The classification behavior of three data is close to each other, where GF-5 has slightly better classification results. In the Landsat-8 classification map, HCF misclassifies sea

into mudflat and paddy into dry land. Dry land and buildings, aquaculture and marsh, pond and aquaculture and marsh and vegetation are confused in the classification map, particularly vegetation are easily misclassified into paddy and marsh. The Sentinel-2 data misclassifies mudflat into buildings. GF-5 data misclassifies sea into pond and paddy into vegetation but it has less misclassification rate than Landsat-8 and Sentinel-2 data. In general, the GF-5 data are slightly more advantageous than Landsat-8 and Sentinel-2 data in classifying 13 land cover types.

Table 7. The comparison of PA and UA between HCF on the Yellow river estuary Landsat-8, Sentinel-2 and GF-5 AHSI data.

	Landsat-8		Sentinel-2		GF-5 AHSI	
	13	21	13	21	13	21
OA (%)	92.34	77.81	93.4	86.15	94.98	97.38
KC	0.90	0.74	0.92	0.84	0.93	0.97

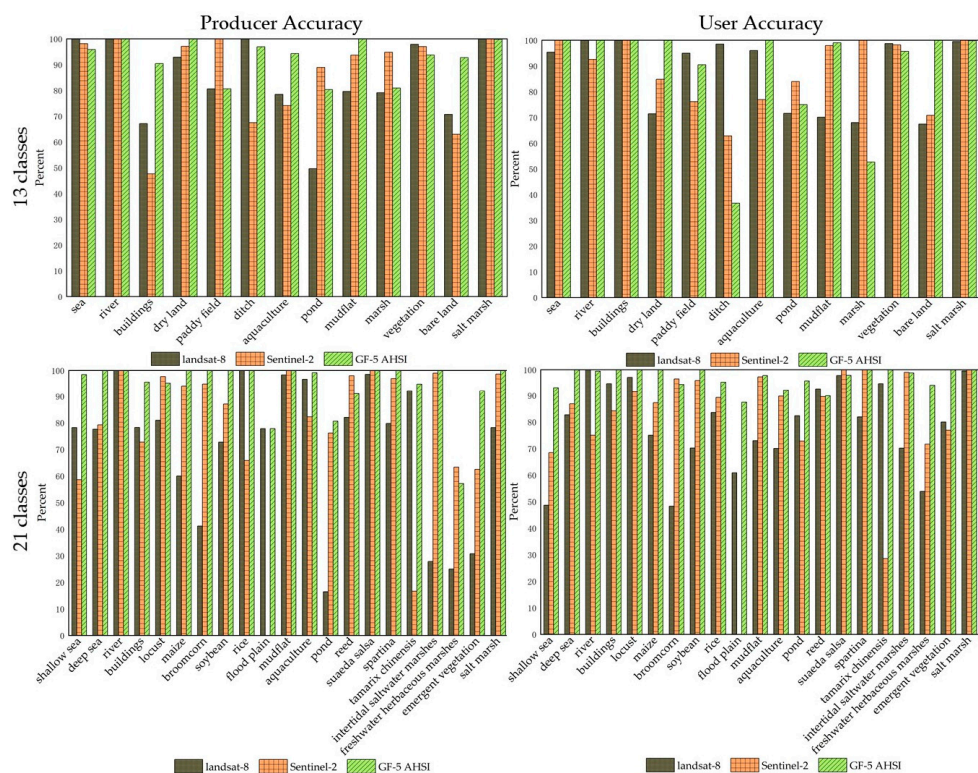


Figure 7. The comparison of PA and UA between HCF on the Yellow river estuary Landsat-8, Sentinel-2 and GF-5 AHSI data.

To further explore different capabilities of GF-5, Landsat-8 and Sentinel-2 data in mapping coastal wetlands, we increase land cover types into 21 classes on the Yellow River estuary data. The 21 classes are shallow sea, deep sea, river, buildings, locust, maize, broomcorn, soybean, rice, flood plain, mudflat, aquaculture, pond, reed, sueda salsa, spartina, tamarix chinensis, intertidal saltwater marshes, freshwater herbaceous marshes, emergent vegetation and salt marsh. As illustrated in Table 7, OA and KC of GF-5 AHSI data are 97.38% and 0.97, the Sentinel-2 are 86.15% and 0.84 and Landsat-8 are 77.81 and 0.74. GF-5 AHSI data has higher OA and KC than Landsat-8 and Sentinel-2 in classifying 21 classes of land cover types. The PA and UA plots in Figure 7 tell that Landsat-8 data has twelve and seven classes with over 80% of UA and PA, Sentinel-2 data has twelve and fourteen, whereas GF-5 has twenty-one and nineteen classes. Especially, 95% of land cover types have over 90% UA and PA in the GF-5 classification map. Moreover, Figure 9 shows classification maps of GF-5, Landsat-8 and Sentinel-2 data. The shallow sea and deep sea, broomcorn and soybean is confused in Landsat-8

classification map. Large areas of Mudflat are misclassified into ponds, spartina, intertidal saltwater marshes and aquaculture are misclassified into ponds. In contrast, fewer misclassification cases exist in GF-5 classification map, with only shallow sea partly misclassified into ponds. In general, GF-5 classification map is the best in both PA and UA. Therefore, we conclude that the GF-5 data has great advantages in fine classification for mapping coastal wetlands.

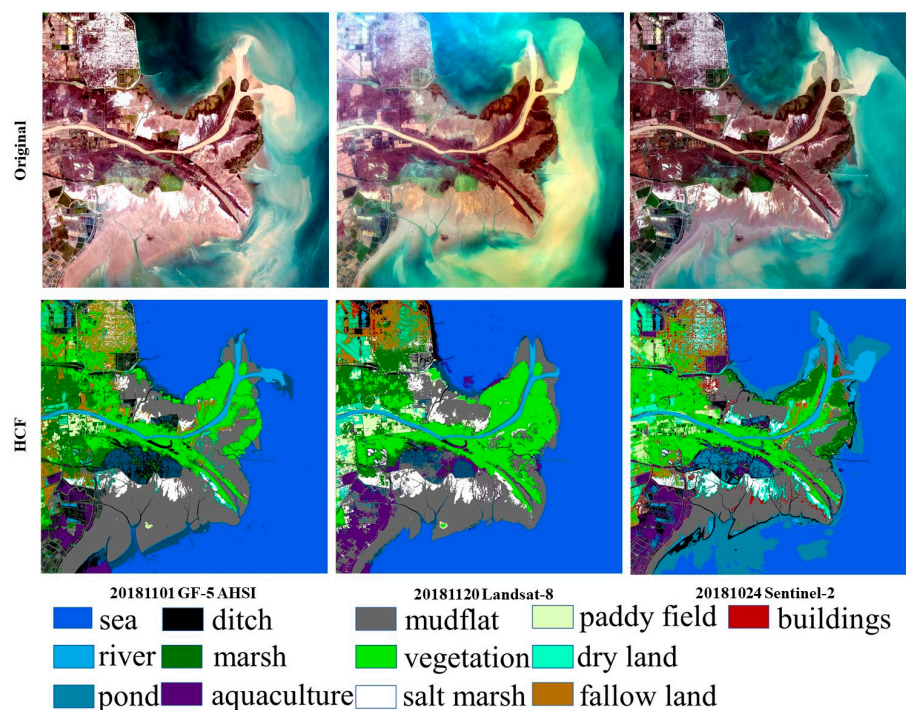


Figure 8. The comparison of 13 land cover types classification maps of Landsat-8, Sentinel-2 and GF-5 data.

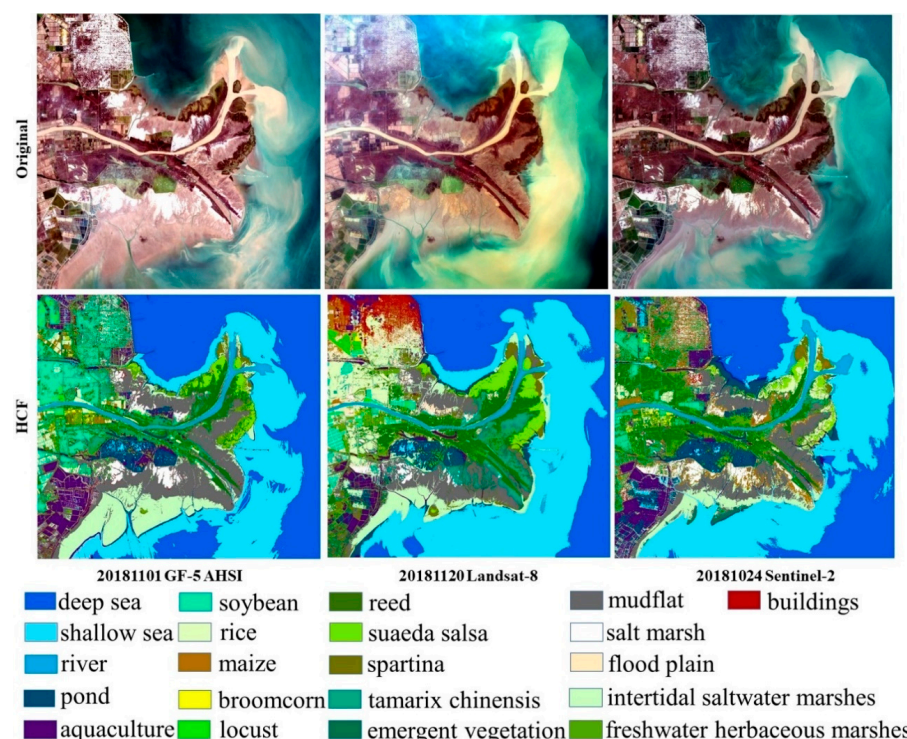


Figure 9. Classification maps of 21 land cover types on Landsat-8, Sentinel-2 and GF-5 data

4.3. Discussions

Considering existing problems in classifying and mapping coastal wetlands, we propose the HCF and design two groups of experiments on two study areas of coastal wetlands. The first group of experiments compares the classification performance of HCF with those of SVM and RF on the Yellow River estuary and Yancheng Landsat images. The HCF has OA above 90% on all Landsat datasets, while the OA of SVM and RF is below 90%. The HCF has lower misclassification rate than of SVM and RF and its UA and PA are obviously superior to those of two comparison methods. Therefore, that HCF achieves better classification accuracies than SVM and RF methods. The SVM and RF are two typical classifiers of machine learning and it owns excellent performance in land cover classification. Unfortunately, land covers in coastal wetlands are complicated and diverse and many different land covers have similar spectral responses with each other. Two classifiers take spectral signals of all samples into the training process and the similar spectrum of different land covers might negatively impact the result of trained classifier. In contrast, our proposed HCF is a hierarchical framework. The first level distinguishes four main classes of land covers using the designed decision tree and the second level combines spectral features, texture features and geometric features and implements SVM to further divide four main classes into fine subtypes of land covers. The first level of HCF adopts expert rules of spectral variables into the decision tree and could reduce confusion or misclassification between different land covers in main classes. The second level adopts the spatial-object information and could well identify different subtypes of land covers in the same main classes. Particularly, in the second level, the classification of each main class is an independent and non-interfering process and it does not require too many training samples, thus reducing the sample asymmetry and promoting the distinguishability among different main classes.

The second group of experiments investigates the classification performance of GF-5 AHSI data, Landsat-8 and Sentinel-2 multispectral data in mapping coastal wetlands using our HCF. When having 13 land cover types, the OA and KC of Landsat-8 are 92.34% and 0.9, Sentinel-2 are 93.4% and 0.92, while those of GF-5 are 94.98% and 0.93. When having 21 land cover types for fine classification, Landsat-8 and Sentinel-2 data have poor behaviors and their OA and KC are reduced to 77.81% and 0.74, 86.15% and 0.84 respectively. In contrast, the OA and KC of GF-5 data do not degrade but increase significantly into 97.38% and 0.97. Therefore, the proposed HCF is also suitable in hyperspectral data and GF-5 data is much advantageous than Sentinel-2 and Landsat-8 in mapping coastal wetlands. Hyperspectral data has the characteristics of numerous bands and narrow spectral range. It accordingly provides approximately continuous spectral information of ground objects and greatly improves the capability in identifying different land covers. GF-5 AHSI data have a spatial resolution of 30 m, same with the Landsat data but it has clear spectral advantages to the Landsat-8 data. When the number of land cover types for classification is small, the spectrum width of Sentinel-2 and Landsat-8 multispectral data could separate different classes. It accordingly has similar classification performance to GF-5 data in classifying the 13 classes of the Yellow River estuary. But when having too many land cover types, the spectral information of Sentinel-2 and Landsat-8 data is too coarse and could not identify some specific similar land cover subtypes (e.g., shallow sea and deep sea). But narrow bands of GF-5 data provide sufficient spectral information, which ensures that it could work well in identifying similar land cover types with subtle spectral divergences. Therefore, compared with Landsat and Sentinel data, the GF-5 data own great advantages in finely mapping coastal wetlands.

Our work in this paper still has some drawbacks and needs further improvements. First, we do not carefully investigate the explanation of selected thresholds in the first level of HCF. Whether the thresholds in the decision tree is reasonable is closely related to the classification accuracy. In the future work, we will try to theoretically explain the selected threshold. Second, the quality of samples is an important factor affecting the classification accuracy. The classification maps still have mixed and misclassified land cover types. Therefore, how to optimize the sample selection is another issue worth exploring in the future. Finally, more satellite remote sensing datasets and deep learning classifiers like cube-pair-based convolutional neural networks (CNN) [71] and CNN-Based Spatial Feature Fusion

Algorithm (CSFF) [72] will be adopted in our framework to further promote the classification behaviors of our HCF.

5. Conclusions

This paper proposes the HCF for mapping coastal wetlands. The HCF includes two levels of classification. The first level adopts the decision tree to roughly categorize land covers into four main classes and the second level implements the SVM classifier on the combined features to obtain fine subtypes of land covers in the same main class. Two groups of experiments on two study areas are designed to testify the classification performance in mapping coastal wetlands and the GF-5 AHSI data and multispectral TM/ETM+/OLI and Sentinel data are implemented. The obtained results were compared with those from two popular methods SVM and RF. Experimental results show that HCF has obvious advantages in classifying land covers of coastal wetlands than SVM and RF, with higher OA and lower misclassification rate. The OA of HCF is all above 90%, whereas that of SVM and RF method is below 90%. UA and PA of HCF are superior to SVM and RF in both the average and individual classes. The classification comparison in Landsat-8, Sentinel-2 and GF-5 data shows that HCF is not only suitable for coarse classification on the multispectral data but also can be applied for fine classification on hyperspectral data. For classifying 13 land cover types, the OA and KC of Landsat-8 are 92.34% and 0.9, Sentinel-2 are 93.4% and 0.92, while those of GF-5 are 94.98% and 0.93. Landsat-8 and Sentinel-2 data have similar behaviors with GF-5 hyperspectral data in making coarse classification of land cover types and GF-5 data is slightly more dominant. When having 21 land cover types, the OA and KC of Landsat-8 are 77.81% and 0.74, Sentinel-2 are 86.15% and 0.84, while those of GF-5 AHSI data reach up to 97.38% and 0.97. The GF-5 data are far superior to Landsat-8 and Sentinel-2 multispectral data in achieving fine classification of coastal wetlands. Therefore, the proposed HCF can be an alternative for mapping coastal wetlands and the GF-5 hyperspectral imagery is a good data source for consideration.

Author Contributions: L.J. analyzed the data, performed the experiments and wrote the draft of the manuscript; W.S. proposed the methodology and revised the manuscript; G.Y. designed the experiments of this study; G.R. and Y.L. gave comments and significantly revised the manuscript.

Funding: This research was funded in part by Open Fund of State Key Laboratory of Remote Sensing Science (Grant No. OFSLRSS201812), in part by the National Natural Science Foundation under Grant 41671342, Grant 41971296 and Grant U1609203, in part by the Natural Science Foundation of Zhejiang Province under Grant LR19D010001 and Grant LQ18D010001, in part by the Ningbo Natural Science Foundation under Grant 2017A610294 and in part by the K. C. Wong Magna Fund from Ningbo University.

Acknowledgments: The authors would like to thank the editor and referees for their suggestions that improve the manuscript.

Conflicts of Interest: The authors declare no conflict of interest.

References

1. Perillo, G.; Wolanski, E.; Cahoon, D.R.; Hopkinson, C.S. *Coastal Wetlands: An Integrated Ecosystem Approach*; Elsevier: New York, NY, USA, 2018.
2. Gabler, C.A.; Osland, M.J.; Grace, J.B.; Stagg, C.L.; Day, R.H.; Hartley, S.B.; Enwright, N.M.; From, A.S.; McCoy, M.L.; McLeod, J.L. Macroclimatic change expected to transform coastal wetland ecosystems this century. *Nat. Clim. Chang.* **2017**, *7*, 142. [[CrossRef](#)]
3. Aslan, A.; Rahman, A.F.; Warren, M.W.; Robeson, S.M. Mapping spatial distribution and biomass of coastal wetland vegetation in Indonesian Papua by combining active and passive remotely sensed data. *Remote Sens. Environ.* **2016**, *183*, 65–81. [[CrossRef](#)]
4. Guo, M.; Li, J.; Sheng, C.; Xu, J.; Wu, L. A review of wetland remote sensing. *Sensors* **2017**, *17*, 777. [[CrossRef](#)] [[PubMed](#)]
5. Tiner, R.W.; Lang, M.W.; Klemas, V.V. *Remote Sensing of Wetlands: Applications and Advances*; CRC Press, Taylor & Francis Group: London, UK, 2015.

6. Woodruff, J.D. *Future of Tidal Wetlands Depends on Coastal Management*; Nature Publishing Group: London, UK, 2018.
7. Lin, Q.; Yu, S. Losses of natural coastal wetlands by land conversion and ecological degradation in the urbanizing Chinese coast. *Sci. Rep.* **2018**, *8*, 15046. [[CrossRef](#)] [[PubMed](#)]
8. Spencer, T.; Schuerch, M.; Nicholls, R.J.; Hinkel, J.; Lincke, D.; Vafeidis, A.; Reef, R.; McFadden, L.; Brown, S. Global coastal wetland change under sea-level rise and related stresses: The DIVA Wetland Change Model. *Glob. Planet. Chang.* **2016**, *139*, 15–30. [[CrossRef](#)]
9. Schuerch, M.; Spencer, T.; Temmerman, S.; Kirwan, M.L.; Wolff, C.; Lincke, D.; McOwen, C.J.; Pickering, M.D.; Reef, R.; Vafeidis, A.T. Future response of global coastal wetlands to sea-level rise. *Nature* **2018**, *561*, 231–234. [[CrossRef](#)]
10. Jiang, T.-T.; Pan, J.-F.; Pu, X.-M.; Wang, B.; Pan, J.-J. Current status of coastal wetlands in China: Degradation, restoration, and future management. *Estuar. Coast. Shelf Sci.* **2015**, *164*, 265–275. [[CrossRef](#)]
11. Murray, N.J. 3 Satellite Remote Sensing for the Conservation of East Asia's Coastal Wetlands. In *Satellite Remote Sensing for Conservation Action: Case Studies from Aquatic and Terrestrial Ecosystems*; Cambridge University Press: Cambridge, UK, 2018.
12. Samiappan, S.; Turnage, G.; Hathcock, L.; Casagrande, L.; Stinson, P.; Moorhead, R. Using unmanned aerial vehicles for high-resolution remote sensing to map invasive Phragmites australis in coastal wetlands. *Int. J. Remote Sens.* **2017**, *38*, 2199–2217. [[CrossRef](#)]
13. Li, N.; Lu, D.; Wu, M.; Zhang, Y.; Lu, L. Coastal wetland classification with multiseasonal high-spatial resolution satellite imagery. *Int. J. Remote Sens.* **2018**, *39*, 8963–8983. [[CrossRef](#)]
14. Ozesmi, S.L.; Bauer, M.E. Satellite remote sensing of wetlands. *Wetl. Ecol. Manag.* **2002**, *10*, 381–402. [[CrossRef](#)]
15. McCarthy, M.J.; Radabaugh, K.R.; Moyer, R.P.; Muller-Karger, F.E. Enabling efficient, large-scale high-spatial resolution wetland mapping using satellites. *Remote Sens. Environ.* **2018**, *208*, 189–201. [[CrossRef](#)]
16. Mahdianpari, M.; Salehi, B.; Mohammadimanesh, F.; Motagh, M. Random forest wetland classification using ALOS-2 L-band, RADARSAT-2 C-band, and TerraSAR-X imagery. *ISPRS J. Photogramm. Remote Sens.* **2017**, *130*, 13–31. [[CrossRef](#)]
17. Bourgeau-Chavez, L.; Endres, S.; Battaglia, M.; Miller, M.; Banda, E.; Laubach, Z.; Higman, P.; Chow-Fraser, P.; Marcaccio, J. Development of a bi-national Great Lakes coastal wetland and land use map using three-season PALSAR and Landsat imagery. *Remote Sens.* **2015**, *7*, 8655–8682. [[CrossRef](#)]
18. Zhang, A.; Sun, G.; Ma, P.; Jia, X.; Ren, J.; Huang, H.; Zhang, X. Coastal wetland mapping with Sentinel-2 MSI imagery based on gravitational optimized multilayer perceptron and morphological attribute profiles. *Remote Sens.* **2019**, *11*, 952. [[CrossRef](#)]
19. Turpie, K.R.; Klemas, V.V.; Byrd, K.; Kelly, M.; Jo, Y.-H. Prospective HypsIRI global observations of tidal wetlands. *Remote Sens. Environ.* **2015**, *167*, 206–217. [[CrossRef](#)]
20. Riaza, A.; Buzzi, J.; García-Meléndez, E.; del Moral, B.; Carrère, V.; Richter, R. Monitoring salt crusts on an AMD contaminated coastal wetland using hyperspectral Hyperion data (Estuary of the River Odiel, SW Spain). *Int. J. Remote Sens.* **2017**, *38*, 3735–3762. [[CrossRef](#)]
21. Alisa, G. The Challenges of Remote Monitoring of Wetlands. *Remote Sens.* **2015**, *7*, 10938–10950.
22. Li, W.; Gong, P. Continuous monitoring of coastline dynamics in western Florida with a 30-year time series of Landsat imagery. *Remote Sens. Environ.* **2016**, *179*, 196–209. [[CrossRef](#)]
23. Han, X.; Chen, X.; Feng, L. Four decades of winter wetland changes in Poyang Lake based on Landsat observations between 1973 and 2013. *Remote Sens. Environ.* **2015**, *156*, 426–437. [[CrossRef](#)]
24. Mleczko, M.; Mróz, M. Wetland mapping using sar data from the sentinel-1a and tandem-x missions: A comparative study in the biebrza floodplain (Poland). *Remote Sens.* **2018**, *10*, 78. [[CrossRef](#)]
25. Ślawik, Ł.; Niedzielko, J.; Kania, A.; Piórkowski, H.; Kopeć, D. Multiple Flights or Single Flight Instrument Fusion of Hyperspectral and ALS Data? A Comparison of their Performance for Vegetation Mapping. *Remote Sens.* **2019**, *11*, 970. [[CrossRef](#)]
26. Kaplan, G.; Avdan, Z.Y.; Avdan, U. Mapping and Monitoring Wetland Dynamics Using Thermal, Optical, and SAR Remote Sensing Data. In *Wetlands Management: Assessing Risk and Sustainable Solutions*; IntechOpen: London, UK, 2019.
27. Stratoulias, D.; Balzter, H.; Zlinszky, A.; Toth, V.R. A comparison of airborne hyperspectral-based classifications of emergent wetland vegetation at Lake Balaton, Hungary. *Int. J. Remote Sens.* **2018**, *17*, 5689–5715. [[CrossRef](#)]

28. McCarthy, M.J.; Colna, K.E.; El-Mezayen, M.M.; Laureano-Rosario, A.E.; Méndez-Lázaro, P.; Otis, D.B.; Toro-Farmer, G.; Vega-Rodriguez, M.; Muller-Karger, F.E. Satellite remote sensing for coastal management: A review of successful applications. *Environ. Manag.* **2017**, *60*, 323–339. [CrossRef] [PubMed]
29. Rebelo, A.J.; Somers, B.; Esler, K.J.; Meire, P. Can wetland plant functional groups be spectrally discriminated? *Remote Sens. Environ.* **2018**, *210*, 25–34. [CrossRef]
30. Hu, Y.; Zhang, J.; Ma, Y.; An, J.; Ren, G.; Li, X. Hyperspectral Coastal Wetland Classification Based on a Multiobject Convolutional Neural Network Model and Decision Fusion. *IEEE Trans. Geosci. Remote Sens. Lett.* **2019**, *16*, 1110–1114. [CrossRef]
31. Cao, F.; Mishra, D.R.; Schalles, J.F.; Miller, W.L. Evaluating ultraviolet (UV) based photochemistry in optically complex coastal waters using the Hyperspectral Imager for the Coastal Ocean (HICO). *Estuar. Coast. Shelf Sci.* **2018**, *215*, 199–206. [CrossRef]
32. Sun, W.; Du, Q. Graph-Regularized Fast and Robust Principal Component Analysis for Hyperspectral Band Selection. *IEEE Trans. Geosci. Remote Sens.* **2018**, *6*, 3185–3195. [CrossRef]
33. Meisam, A.; Bahram, S.; Sahel, M.; Brisco, B. Spectral analysis of wetlands using multi-source optical satellite imagery. *ISPRS J. Photogramm. Remote Sens.* **2018**, *144*, 119–136.
34. Adam, E.; Mutanga, O. Spectral discrimination of papyrus vegetation (*Cyperus papyrus* L.) in swamp wetlands using field spectrometry. *ISPRS J. Photogramm. Remote Sens.* **2015**, *64*, 612–620.
35. Colditz René, R.; Troche Souza, C.; Vazquez, B.; Wickel, A.J.; Ressl, R. Analysis of optimal thresholds for identification of open water using MODIS-derived spectral indices for two coastal wetland systems in Mexico. *Int. J. Appl. Earth Obs. Geoinf.* **2018**, *64*, 612–620. [CrossRef]
36. Han, X.; Pan, J.; Devlin, A.T. Remote sensing study of wetlands in the Pearl River Delta during 1995–2015 with the support vector machine method. *Front. Earth Sci.* **2018**, *12*, 521–531. [CrossRef]
37. Liu, J.; Feng, Q.; Gong, J.; Zhou, J.; Li, Y. Land-cover classification of the Yellow River Delta wetland based on multiple end-member spectral mixture analysis and a Random Forest classifier. *Int. J. Remote Sens.* **2016**, *37*, 1845–1867. [CrossRef]
38. Reschke, J.; Hüttich, C. Continuous field mapping of Mediterranean wetlands using sub-pixel spectral signatures and multi-temporal Landsat data. *Int. J. Appl. Earth Obs. Geoinf.* **2014**, *28*, 220–229. [CrossRef]
39. Petropoulos, G.P.; Kalivas, D.P.; Griffiths, H.M.; Dimou, P.P. Remote sensing and GIS analysis for mapping spatio-temporal changes of erosion and deposition of two Mediterranean river deltas: The case of the Axios and Aliakmonas rivers, Greece. *Int. J. Appl. Earth Obs. Geoinf.* **2015**, *35*, 217–228. [CrossRef]
40. Dubeau, P.; King, D.; Unbushe, D.; Rebelo, L.-M. Mapping the Dabus wetlands, Ethiopia, using random forest classification of Landsat, PALSAR and topographic data. *Remote Sens.* **2017**, *9*, 1056. [CrossRef]
41. Dronova, I. Object-based image analysis in wetland research: A review. *Remote Sens.* **2015**, *7*, 6380–6413. [CrossRef]
42. Cao, J.; Leng, W.; Liu, K.; Liu, L.; He, Z.; Zhu, Y. Object-based mangrove species classification using unmanned aerial vehicle hyperspectral images and digital surface models. *Remote Sens.* **2018**, *10*, 89. [CrossRef]
43. Berberoğlu, S.; Akin, A.; Atkinson, P.; Curran, P. Utilizing image texture to detect land-cover change in Mediterranean coastal wetlands. *Int. J. Remote Sens.* **2010**, *31*, 2793–2815. [CrossRef]
44. Jia, M.; Wang, Z.; Li, L.; Song, K.; Ren, C.; Liu, B.; Mao, D. Mapping China's mangroves based on an object-oriented classification of Landsat imagery. *Wetlands* **2014**, *34*, 277–283. [CrossRef]
45. Wang, M.; Fei, X.; Zhang, Y.; Chen, Z.; Wang, X.; Tsou, J.; Liu, D.; Lu, X. Assessing texture features to classify coastal wetland vegetation from high spatial resolution imagery using completed local binary patterns (CLBP). *Remote Sens.* **2018**, *10*, 778. [CrossRef]
46. Gu, Y.; Liu, T.; Jia, X.; Benediktsson, J.A.; Chanussot, J. Nonlinear multiple kernel learning with multiple-structure-element extended morphological profiles for hyperspectral image classification. *IEEE Trans. Geosci. Remote Sens.* **2016**, *54*, 3235–3247. [CrossRef]
47. Wang, Q.; He, X.; Li, X. Locality and Structure Regularized Low Rank Representation for Hyperspectral Image Classification. *IEEE Trans. Geosci. Remote Sens.* **2019**, *57*, 911–923. [CrossRef]
48. Cao, X.; Zhou, F.; Xu, L.; Meng, D.; Xu, Z.; Paisley, J. Hyperspectral image classification with Markov random fields and a convolutional neural network. *IEEE Trans. Image Process.* **2018**, *27*, 2354–2367. [CrossRef] [PubMed]

49. Belgiu, M.; Drăguț, L. Random forest in remote sensing: A review of applications and future directions. *ISPRS J. Photogramm. Remote Sens.* **2016**, *114*, 24–31. [[CrossRef](#)]
50. Sun, W.; Du, B.; Xiong, S. Quantifying sub-pixel surface water coverage in urban environments using low-albedo fraction from Landsat imagery. *Remote Sens.* **2017**, *9*, 428. [[CrossRef](#)]
51. Zhu, C.; Zhang, X.; Huang, Q. Four Decades of Estuarine Wetland Changes in the Yellow River Delta Based on Landsat Observations Between 1973 and 2013. *Water* **2018**, *10*, 933. [[CrossRef](#)]
52. Cui, B.-L.; Li, X.-Y. Coastline change of the Yellow River estuary and its response to the sediment and runoff (1976–2005). *Geomorphology* **2011**, *127*, 32–40. [[CrossRef](#)]
53. Liu, G.; Zhang, L.; Zhang, Q.; Musyimi, Z.; Jiang, Q. Spatio-temporal dynamics of wetland landscape patterns based on remote sensing in Yellow River Delta, China. *Wetlands* **2014**, *34*, 787–801. [[CrossRef](#)]
54. Zhu, C.; Zhang, X. Coastal Remote Sensing. In *Modeling with Digital Ocean and Digital Coast*; Springer International Publishing: New York, NY, USA, 2017; pp. 169–203.
55. Liu, X.; Liu, H.; Lin, Z.; Li, L.; Lv, S. Spatial pattern changes of Spartina alterniflora with different invasion ages in the Yancheng coastal wetland. *Acta Ecol. Sin.* **2017**, *37*, 307–314. [[CrossRef](#)]
56. Zhang, H.; Liu, H.; Hou, M.; Li, Y. Building model based on processes and simulating landscape change in the coastal wetlands—A case study of the core area in Yancheng Natural Reserve. *J. Nat. Resour.* **2014**, *29*, 1105–1115.
57. Ke, C.-Q.; Zhang, D.; Wang, F.-Q.; Chen, S.-X.; Schmullius, C.; Boerner, W.-M.; Wang, H. Analyzing coastal wetland change in the Yancheng national nature reserve, China. *Reg. Environ. Chang.* **2011**, *11*, 161–173. [[CrossRef](#)]
58. Chen, C.-F.; Lau, V.-K.; Chang, N.-B.; Son, N.-T.; Chiang, S.-H. Multi-temporal change detection of seagrass beds using integrated Landsat TM/ETM+/OLI imageries in Cam Ranh Bay, Vietnam. *Ecol. Inf.* **2016**, *35*, 43–54. [[CrossRef](#)]
59. Immitzer, M.; Vuolo, F.; Atzberger, C. First Experience with Sentinel-2 Data for Crop and Tree Species Classifications in Central Europe. *Remote Sens.* **2016**, *8*, 166. [[CrossRef](#)]
60. Wang, Q.; Lin, J.; Yuan, Y. Salient Band Selection for Hyperspectral Image Classification via Manifold Ranking. *IEEE Trans. Neural Netw. Learn.* **2016**, *27*, 1279–1289. [[CrossRef](#)] [[PubMed](#)]
61. Tan, Y.; Sun, J.Y.; Zhang, B.; Chen, M.; Liu, Y.; Liu, X.D. Sensitivity of a Ratio Vegetation Index Derived from Hyperspectral Remote Sensing to the Brown Planthopper Stress on Rice Plants. *Sensors* **2019**, *19*, 375. [[CrossRef](#)] [[PubMed](#)]
62. Pringle, M.J.; Schmidt, M.; Tindall, D.R. Multi-decade, multi-sensor time-series modelling—Based on geostatistical concepts—To predict broad groups of crops. *Remote Sens. Environ.* **2018**, *216*, 183–200. [[CrossRef](#)]
63. Visser, F.; Buis, K.; Verschoren, V.; Schoelynck, J. Mapping of submerged aquatic vegetation in rivers from very high-resolution image data, using object-based image analysis combined with expert knowledge. *Hydrobiologia* **2016**, *812*, 157–175. [[CrossRef](#)]
64. Gravey, M.; Rasera, L.G.; Mariethoz, G. Analogue-based colorization of remote sensing images using textural information. *ISPRS J. Photogramm. Remote Sens.* **2019**, *147*, 242–254. [[CrossRef](#)]
65. Zhang, C.; Mishra, D.R.; Pennings, S.C. Mapping salt marsh soil properties using imaging spectroscopy. *ISPRS J. Photogramm. Remote Sens.* **2019**, *148*, 221–234. [[CrossRef](#)]
66. Sulla-Menashe, D.; Gray, J.M.; Abercrombie, S.P.; Tarantino, C.; Blonda, P.; Tomaselli, V.; Kunin, W.E. Hierarchical mapping of annual global land cover 2001 to present: The MODIS Collection 6 Land Cover product. *Remote Sens. Environ.* **2019**, *222*, 183–194. [[CrossRef](#)]
67. Gavish, Y.; O’Connell, J.; Marsh, C.J.; Tarantino, C.; Blonda, P.; Tomaselli, V.; Kunin, W.E. Comparing the performance of flat and hierarchical Habitat/Land-Cover classification models in a NATURA 2000 site. *ISPRS J. Photogramm. Remote Sens.* **2018**, *136*, 1–12. [[CrossRef](#)]
68. Hou, X.; Feng, L.; Chen, X.; Zhang, Y. Dynamics of the wetland vegetation in large lakes of the Yangtze Plain in response to both fertilizer consumption and climatic changes. *ISPRS J. Photogramm. Remote Sens.* **2018**, *141*, 148–160. [[CrossRef](#)]
69. Kamal, M.; Phinn, S. Hyperspectral Data for Mangrove Species Mapping: A Comparison of Pixel-Based and Object-Based Approach. *Remote Sens.* **2011**, *3*, 2222–2242. [[CrossRef](#)]
70. Clark, M.L.; Kilham, N.E. Mapping of land cover in northern California with simulated hyperspectral satellite imagery. *ISPRS J. Photogramm. Remote Sens.* **2016**, *119*, 228–245. [[CrossRef](#)]

71. Wei, W.; Zhang, J.; Zhang, L.; Tian, C.; Zhang, Y. Deep cube-pair network for hyperspectral imagery classification. *Remote Sens.* **2018**, *10*, 783. [[CrossRef](#)]
72. Wang, Q.; Yuan, Z.; Li, X. GETNET: A General End-to-end Two-dimensional CNN Framework for Hyperspectral Image Change Detection. *IEEE Trans. Geosci. Remote Sens.* **2019**, *57*, 3–13. [[CrossRef](#)]



© 2019 by the authors. Licensee MDPI, Basel, Switzerland. This article is an open access article distributed under the terms and conditions of the Creative Commons Attribution (CC BY) license (<http://creativecommons.org/licenses/by/4.0/>).